European Radiology (2019) 29:3782–3790
https://doi.org/10.1007/s00330-019-06144-5

GASTROINTESTINAL

The value of single-source dual-energy CT imaging for discriminating microsatellite instability from microsatellite stability human colorectal cancer

Jingjun Wu[1] · Yue Lv[1] · Nan Wang[1] · Ying Zhao[1] · Pengxin Zhang[2] · Yijun Liu[1] · Anliang Chen[1] · Jianying Li[3] · Xin Li[3] · Yan Guo[3] · Tingfan Wu[3] · Ailian Liu[1]

Received: 21 December 2018 / Revised: 22 February 2019 / Accepted: 8 March 2019 / Published online: 22 March 2019

Abstract

Objectives To demonstrate the value of single-source dual-energy computed tomography (ssDECT) imaging for discriminating microsatellite instability (MSI) from microsatellite stability (MSS) colorectal cancer (CRC).

Methods Thirty-eight and seventy-six patients with pathologically proven MSI and MSS CRC, respectively, were retrospectively selected and compared. These patients underwent contrast-enhanced abdominal ssDECT scans before any anti-cancer treatment. Effective atomic number (Eff-Z) in precontrast phase, slope *k* of spectral HU curve in precontrast (*k*-P), arterial (*k*-A), venous (*k*-V), and delayed phase (*k*-D), normalized iodine concentration in arterial (NIC-A), venous (NIC-V), and delayed phase (NIC-D), of tumors in two groups were measured by two reviewers. Consistency of measurements was tested by intra-class correlation coefficients (ICC). Mann-Whitney *U* test or Student's *t* test was used to compare above values between MSI and MSS. Multivariate logistic regression was used to analyze multiple parameters. Receiver operating characteristic curves were calculated to assess diagnostic efficacies.

Results Interobserver agreement was excellent (ICC > 0.80). MSI CRC had significantly lower values in all measurements (NIC-A, V, D; *k*-P, A, V, D; Eff-Z) than MSS CRC. For discriminating MSI from MSS CRC, the area under curve (AUC) using *k*-A was the highest (AUC, 0.803; sensitivity, 72.4%; specificity, 76.3%). The multivariate logistic regression (selection method, Enter) with combined ssDECT parameters (NIC-A, NIC-V, NIC-D, Eff-Z, *k*-P, *k*-A, *k*-V, *k*-D) significantly improved diagnostic capability with AUC of 0.886 (sensitivity, 81.6%; specificity, 81.6%).

Conclusions The combination of multiple parameters in ssDECT imaging by multivariate logistic regression provides relatively high diagnostic accuracy for discriminating MSI from MSS CRC.

Key Points

- *ssDECT generates multiple parameters for discriminating CRC with MSI from MSS.*
- *ssDECT measurements for MSI CRC were significantly lower than MSS CRC.*
- *Combination of ssDECT parameters further improves diagnostic capability for differentiation.*

Keywords Microsatellite instability · Colorectal neoplasms · Radiography, dual-energy scanned projection

Jingjun Wu and Yue Lv contributed equally to this work.

Electronic supplementary material The online version of this article (https://doi.org/10.1007/s00330-019-06144-5) contains supplementary material, which is available to authorized users.

✉ Ailian Liu
cjr.liuailian@vip.163.com

[1] Department of Radiology, The First Affiliated Hospital of Dalian Medical University, Xigang district, Zhongshan road, No.222, Dalian, China

[2] Department of Pathology, The First Affiliated Hospital of Dalian Medical University, Xigang district, Zhongshan road, No.222, Dalian, China

[3] GE Healthcare, NO.1 Tongji South Road Beijing Economic Technology Development Area, Beijing, China

Abbreviations

AUC	Area under the curve
CRC	Colorectal cancer
DNA	Deoxyribonucleic acid
Eff-Z	Effective atomic number
GSI	Gemstone Spectral Imaging
IC	Iodine concentration
ICC	Intra-class correlation coefficients
IHC	Immunohistochemistry
MMR	Mismatch repair
MRI	Magnetic resonance imaging
MSI	Microsatellite instability
MSS	Microsatellite stability
NIC	Normalized iodine concentration
PCR	Polymerase chain reaction
PET-CT	Positron emission tomography/computed tomography
ROI	Region of interest
ssDECT	Single-source dual-energy computed tomography

Introduction

Colorectal cancer (CRC) is one of the leading causes of cancer related death among both men and women, causing about 700,000 deaths every year worldwide [1].

Among various CRC patients, the distinct heterogeneity of prognosis and treatment response has been observed in clinical practice, even for those who experienced similar pathological stages and treatment modalities. Microsatellite instability (MSI) is one of the robust biomarkers to predict CRC outcome. MSI is caused by replication errors of microsatellite deoxyribonucleic acid (DNA), a simple sequence repeat consisting of a 2–6 base tandem structure [2]. In normal tissues, the mismatch repair (MMR) system can repair DNA replication errors. For several oncogenic tissues, MMR system is deficient (caused by dysfunction of any MMR protein including hMLH1, hMSH2, hMSH6, and hPMS2), and will block the normal repair process of replication errors, resulting in the accumulation of false sequences and microsatellite DNA instability [3]. The 2017 guideline of the updated National Comprehensive Cancer Network clinical practice has pointed out that MSI CRC patients can benefit from immunotherapy like anti-PD1 (anti-programmed death-1) and anti-CTLA-4 (anti-cytotoxic T Lymphocyte associated antigen-4) with a likely better prognosis, while they cannot benefit from fluorouracil chemotherapy [4, 5]. Obtaining MSI status is meaningful for CRC treatment strategies. Clinically, MSI detection relies on the patient's pathological specimens via polymerase chain reaction (PCR) or immunohistochemistry (IHC) test, however, these advanced biological tests may be available only in tertiary centers, not necessarily in local facilities, which makes it not widely available to ascertain MSI status [6]. Colonoscopic biopsy is the proper way to obtain CRC tissues, however the tumors are heterogeneous, and colonoscopy can only capture a small portion of the tissue samples [7]. Thus, it is useful to explore a non-invasive method to discriminate MSI from microsatellite stability (MSS) CRCs.

The single-source dual-energy computed tomography (ssDECT) generates multiparametric images. The effective atomic number (Eff-Z) can quantitatively describe the changes of X-ray absorption rate for different substances and is best used in non-contrast enhanced scans. The iodine concentration (IC) measured in the material-decomposition images such as iodine-based images in contrast-enhanced scans can be used to quantitatively reflect the blood flow [8]. Studies have demonstrated the clinical values of ssDECT in grading CRC, assessing regression after neoadjuvant treatment, evaluating Ki-67 and hypoxia-inducible factor 1α, and as an alternative to perfusion CT [9–12]. MSI and MSS CRC tissues are at different angiogenesis levels and have different cellular densities [13, 14]. Our hypothesis was that the difference in angiogenesis may be demonstrated with iodine-based images and reflected by changes of spectral curves in contrast-enhanced images. Also, we questioned if the different cellular densities may be reflected by Eff-Z in non-enhancement scans. The purpose of our study was thus to demonstrate the value of ssDECT imaging in discriminating MSI from MSS CRCs.

Materials and methods

Patients

Our institutional review board approved this retrospective study, and the requirement for informed consent was waived. From January 2016 to July 2018, the 38 MSI CRC patients and 76 MSS CRC patients (62 males, 52 females; aged 62.45 ± 11.29 years; ranged 26–83 years) who met the following criteria were identified and enrolled in our study. The inclusion criteria were (1) diagnosed as CRC by postoperative pathology, (2) underwent routine abdominal enhanced ssDECT before surgical resection within 2 weeks; and (3) with available postoperative specimens for IHC staining to test MSI status. The exclusion criteria were (1) with any anti-cancer therapy (radiotherapy, chemotherapy, biotherapy) before imaging and surgery; (2) with invisible target lesion on CT images; (3) poor image quality (poor signal-to-noise ratio, or severe bowel motion artifacts). Detailed patient information is listed in Table 1.

Single-source dual-energy CT imaging

All abdominal ssDECT scans were performed on a Discovery CT750HD scanner (GE Healthcare) in supine position. The dual-energy CT scan parameters were as follows: rapid switching between tube voltages of 80 kVp and 140 kVp; tube current, 375 mA; helical pitch, 1.375:1; rotation time, 0.8 s.

Table 1 Demographics of the CRC patients

Characteristic		Number (%)
All patients enrolled		114 (100)
Age (year)	Mean ± SD	62.45 ± 11.29
	Range	26–83
Gender	Male	62 (54.4)
	Female	52 (45.6)
Tumor size (cm)	Median	1.70
	(25th, 75th percentiles)	(1.30, 2.20)
Tumor location	Right colon	37 (32.5)
	Left colon	41 (36.0)
Pathological general types	Rectum	36 (31.5)
	Mass type	47 (41.2)
	Infiltration type	2 (1.8)
	Ulcer type	65 (57.0)
CEA	Normal	64 (56.1)
	Abnormal	50 (43.9)
CA19-9	Normal	93 (81.6)
	Abnormal	21 (18.4)
Differentiation grade	High	13 (11.4)
	Moderate	87 (76.3)
	Low	14 (12.3)
T stage	T1	1 (0.9)
	T2	19 (16.6)
	T3	5 (4.4)
	T4	89 (78.1)
N stage	N0	73 (64)
	N1	31 (27.2)
	N2	10 (8.8)

CRC colorectal cancer, *CEA* carcino-embryonicantigen, *CA19-9* carbohydrate antigen 19-9, *N* lymph node, *T* tumor

The non-enhanced abdominal scan was acquired first. After the non-contrast CT scan, the non-ionic contrast media iohexol (Omnipaque 300 mg/mL, GE Healthcare) was injected at a patient weight-dependent dose of 1.2 mL/kg and injection rate of 3–3.5 ml/s through median cubital vein, followed by flushing of 40 mL saline at the same rate. At 30, 60, and 120 s after the start of contrast injection, the arterial phase, venous phase, and delayed phase contrast-enhanced CT scans were performed.

Image generation and analysis

After the CT scans, two types of dual-energy CT images were reconstructed at 2.5 mm image slice thickness and interval: the 101 sets of virtual monochromatic spectral images (photon energy levels from 40 to 140 keV) and iodine-based material decomposition images. These images were transferred to an advanced workstation 4.6 (AW 4.6; GE Healthcare) for measurement and analysis using the Gemstone Spectral Imaging (GSI) viewer software. Image analysis was performed by two abdominal radiologists with 5 years of experience in abdominal imaging, and these two radiologists were blinded to all clinical and pathological information (the postprocessing of each case took about 5 min by every radiologist). First, the two radiologists observed and analyzed all images, and selected the 70 keV monochromatic image in the arterial phase to place a region of interest (ROI) at least 10 mm^2 on the solid areas (avoiding bleeding, necrosis, and cystic portions) of the tumor at the slice with the largest axial diameter of tumor, and again on its adjacent upper and lower slices (for calculating the average). The average values were calculated to minimize measurement bias. The corresponding ROI was then propagated to images of all energies in the precontrast, venous, and delayed phases to be consistent. The same ROI was also propagated to the iodine-based material decomposition image, which is photon energy-independent. The mean area of all ROIs was 34.26 mm^2; range, 10.58–153.85 mm^2.

Using the GSI viewer software package, the tumor Eff-Z in the precontrast phase was generated. The tumor CT value measurement as function of photon energy in the precontrast, arterial, venous, and delayed phase was used to generate the spectral HU curve (*x*-axis represents the energy from 40 to 140 keV, *y*-axis represents the mean CT value), and to calculate the curve slopes (*k*): $k = (\text{CT value (40 keV)} - \text{CT value (100 keV)})/60$. The IC value of tumor was measured on the iodine-based material decomposition image. To minimize variations caused by individual differences in cardiac function and blood flow dynamics between patients, the IC value of arteries (external iliac arteries in rectal cancer patients, and aorta ventralis in colon cancer patients) at the same slice of the tumors was measured to calculate the normalized iodine concentration (NIC) for tumors using the following formula: $\text{NIC} = \text{IC}_{\text{tumor}}/\text{IC}_{\text{artery}}$. To minimize measurement bias, the measurements from the two radiologists were averaged to produce the final result and the original data were tested for consistency. The examples of ssDECT images and the ROIs for the assessment of the quantitative measurements are shown in Figs. 1 and 2.

IHC test for MMR proteins

Four micrometer sections were cut from the postoperative paraffin-embedded specimens and then deparaffinized. Dehydration and antigen retrieval were performed by gradient alcohol and high pressure, respectively. After preincubation by 3% hydrogen peroxide solution (10 min) at room temperature, the sections were stained with monoclonal mouse anti-human hMLH1, hMSH2, hMSH6, and hPMS2 antibody (Ventana medical systems inc.,) at 4 °C overnight. The secondary goat anti-mouse antibody (Beijing Zhongshan Golden Bridge Biotechnology Company) was incubated for 30 min at 37 °C. The biotin-horseradish peroxidase complex (1:100 dilution) was then incubated for 20 min at room temperature. Then, the

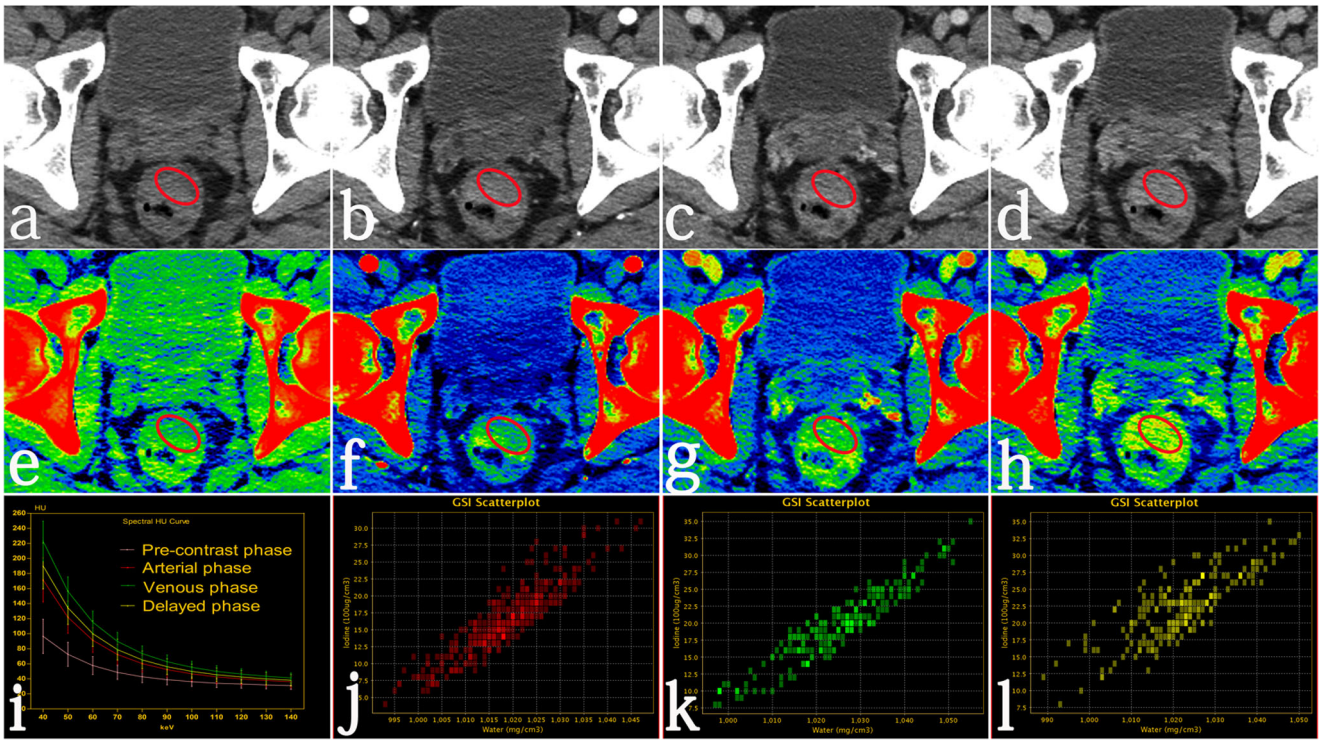

Fig. 1 Images of a 47-year-old male with histopathologically proved MSI rectal cancer. The examples of regions of interest (ROIs) are shown on 70 KeV monochromatic CT images in the precontrast (**a**), arterial (**b**), venous (**c**), and delayed phase (**d**). And the same ROIs are also propagated to the effective atomic number image in precontrast phase (Eff-Z = 7.86) (**e**), and iodine-based material decomposition images in arterial (**f**), venous (**g**), and delayed phase (**h**. **j**, **k**, **l**) show scatter diagrams of iodine concentration (IC) of ROI: IC = 15.40, 19.76, and 17.95 μg/cm^3 in arterial (**j**), venous (**k**), and delayed phase (**l**). The IC of the artery is 136.31, 42.31, and 30.67 μg/cm^3, and normalized IC = 0.113 (15.40/136.31), 0.467 (19.76/42.31), and 0.585 (17.95/30.67) in arterial, venous, and delayed phase, respectively. The spectral Hounsfield unit curves are generated with curve slopes of 1.005, 2.079, 2.793, and 2.336 in precontrast, arterial, venous, and delayed phase (**i**)

sections were stained by 3–3′-diaminobenzine-tetrahydrochloride, counterstained by hematoxylin, and observed under microscope. Negative control group: the primary antibody was discarded and replaced by phosphate buffer saline.

The evaluation of the results of IHC for MMR proteins was performed by two trained pathologists who were blinded to the patients' any clinical and pathological diagnosis. The unanimous opinions were acquired. If there were different opinions, a third pathologist participated in consultation and achieved consistent view. Positive staining of hMLH1, hMSH2, hMSH6, and hPMS2 were localized with brown nuclear staining (Fig. 3). Criterion for evaluating MSI status was as follows: MSI, at least one of the four proteins was negatively stained, namely, deficient MMR; MSS, all of these four proteins were positively stained, namely, proficient MMR [15, 16].

Statistical analysis

Statistical analysis was performed using SPSS 22.0 software package (SPSS Inc). The Shapiro-Wilk test was used to check normality. Normally distributed data were analyzed by Student's *t* test, and were expressed as means ± standard deviations. Non-normally distributed data were analyzed by Mann-Whitney *U* test, and were expressed as medians and ranges (25th, 75th percentiles). $P < 0.05$ was considered as statistically significant. The consistencies of the measurements between the two observers were tested using intra-class correlation coefficients (ICC) (model, two-way random; type, average absolute agreement). The significant ssDECT parameters were combined by multivariate logistic regression to improve the diagnostic capabilities. Seven selection methods in multivariate logistic regression ("Enter," "Forward: Conditional," "Forward: LR," "Forward: Wald," "Backward: Conditional," "Backward: LR," and "Backward: Wald") were used to obtain the optimal method for discriminating MSI from MSS CRC. The receiver operating characteristic (ROC) analysis was used to compare diagnostic capabilities. The area under the curve (AUC), sensitivity, specificity, cutoff value, and 95% CI were calculated. Delong test was used to compare the difference between AUCs.

Results

Interobserver agreement

The consistencies of all measurements between two observers were excellent with ICC values greater than 0.80. The ICC values of NIC in arterial (NIC-A), venous (NIC-V), and delayed

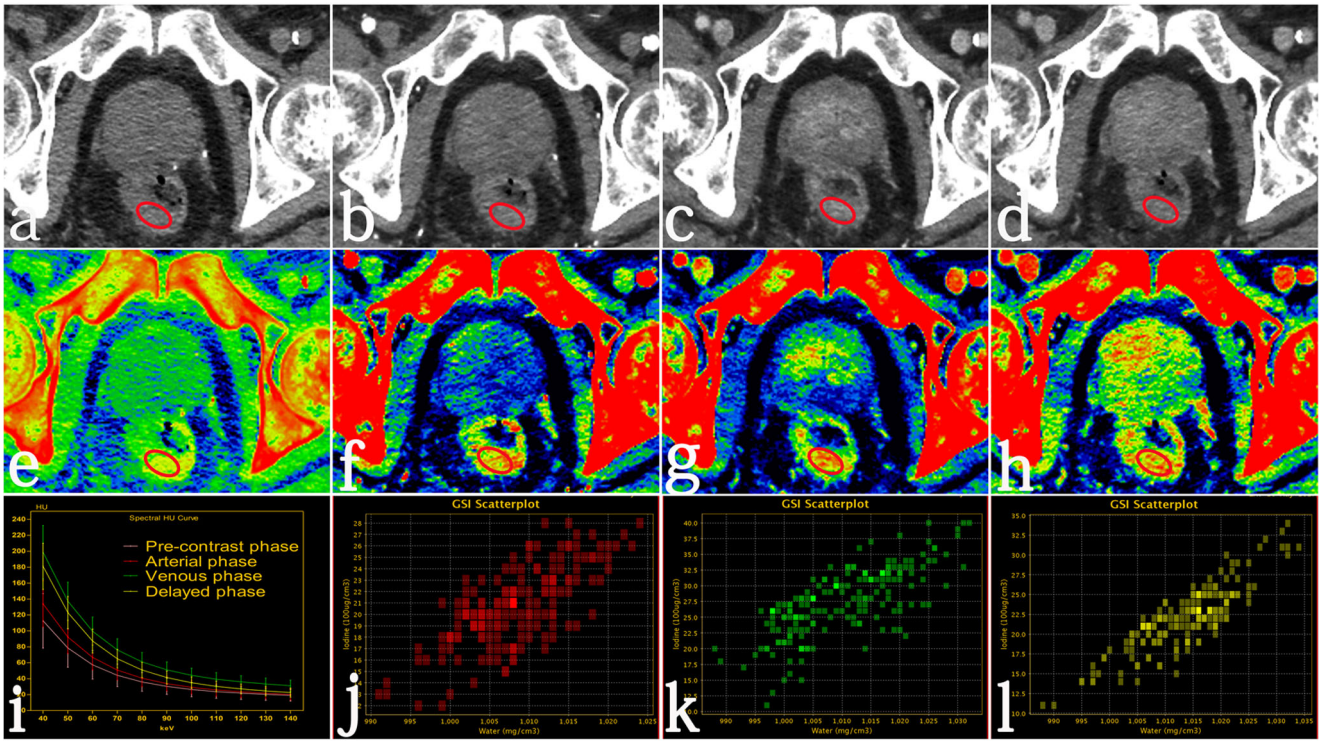

Fig. 2 Images of a 76-year-old male with histopathologically proved MSS rectal cancer. The examples of regions of interest (ROIs) are shown on 70 KeV monochromatic CT images in the precontrast (**a**), arterial (**b**), venous (**c**), and delayed phase (**d**). And the same ROIs are also propagated to the effective atomic number image in precontrast phase (Eff-Z = 8.74) (**e**), and iodine-based material decomposition images in arterial (**f**), venous (**g**), and delayed phase (**h**). **j**, **k**, **l** show scatter diagrams of iodine concentration (IC) of ROI: IC = 20.69, 27.46, and 21.95 μg/cm^3 in arterial (**j**), venous (**k**), and delayed phase (**l**). The IC of the artery is 156.56, 41.84, and 31.46 μg/cm^3, and normalized IC = 0.132 (20.69/156.56), 0.656 (27.46/41.84), and 0.698 (21.95/31.46) in arterial, venous, and delayed phase, respectively. The spectral Hounsfield unit curves are generated with curve slopes of 1.437, 1.747, 2.577, and 2.437 in precontrast, arterial, venous, and delayed phase (i)

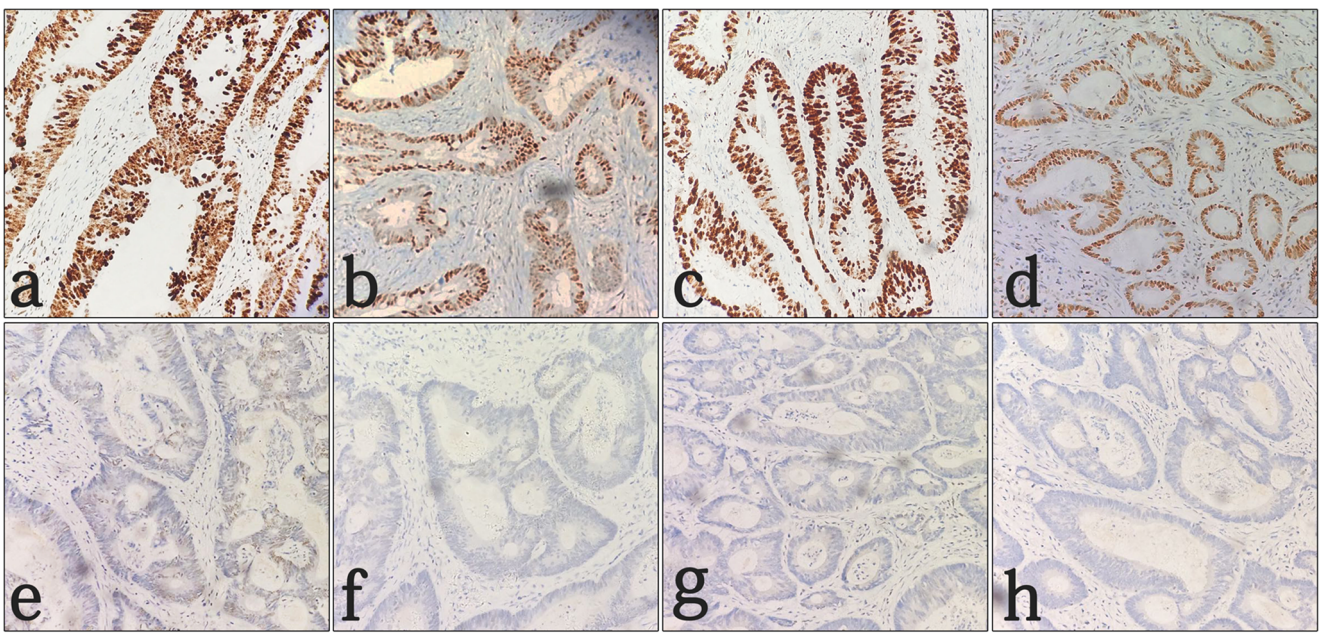

Fig. 3 Immunohistochemical staining of mismatch repair (MMR) proteins to assess MSI status. MMR proteins include hMLH1 (**a**, **e**), hMSH2 (**b**, **f**), hMSH6 (**c**, **g**), and hPMS2 (**d**, **h**). Positive expressions of MMR proteins are localized with brown nuclear stainings (**a**–**d**), and negative expressions are without nuclear stainings (**e**–**h**). When at least one of the four MMR proteins is negatively stained, it is defined as MSI, and when there are four positively stained MMR proteins, it is defined as MSS. All magnifications are × 200

phase (NIC-D), Eff-Z, slope *k* in precontrast (*k*-P), arterial (*k*-A), venous (*k*-V), and delayed phase (*k*-D) were 0.937, 0.935, 0.907, 0.925, 0.932, 0.936, 0.900, and 0.856, respectively.

Relationship between ssDECT parameters and MSI status

NIC values of MSI CRC were significantly lower than those of MSS CRC in arterial phase, venous phase, and delayed phase (all $p < 0.001$). The slope *k* values of the spectral HU curves in MSI CRC were significantly lower than those in MSS CRC in the precontrast phase ($p = 0.001$), arterial phase, venous phase, and delayed phase (all $p < 0.001$) (Fig. 4). The Eff-Z value of MSI CRC in the precontrast phase was also significantly lower than that of MSS CRC ($p = 0.001$). The detailed NIC, Eff-Z, and slope *k* values for MSI and MSS CRC patients are shown in Table 2.

Diagnostic capabilities of ssDECT parameters to discriminate MSI from MSS CRC

The AUC of using the slope *k* value in the arterial phase was 0.803 (sensitivity, 72.4%; specificity, 76.3%; cutoff value, 2.00). The AUC of using *k*-A was significantly higher than that of using Eff-Z, *k*-P, and *k*-D ($p = 0.014$, 0.018, 0.014, respectively). The AUC of using *k*-A was higher than that of

Table 2 NIC, Eff-Z, and *k* values for MSI and MSS CRC patients

Parameters	MSI	MSS	*p* value
NIC-A	0.102 (0.074, 0.129)	0.141 (0.115, 0.163)	< 0.001
NIC-V	0.400 (0.322, 0.466)	0.524 (0.427, 0.652)	< 0.001
NIC-D	0.510 (0.400, 0.636)	0.693 (0.527, 0.815)	< 0.001
Eff-Z	7.880 (7.825, 8.030)	8.040 (7.870, 8.138)	0.001
k-P	0.557 (0.458, 0.811)	0.834 (0.526, 1.040)	0.001
k-A	1.513 (1.206, 1.996)	2.454 (1.936, 2.930)	< 0.001
k-V	2.04 ± 0.57	2.70 ± 0.63	< 0.001
k-D	1.96 ± 0.56	2.36 ± 0.51	< 0.001

A arterial phase, *D* delayed phase, *Eff-Z* effective atomic numbers, *k* slope, *MSI* microsatellite instability, *MSS* microsatellite stability, *NIC* normalized iodine concentration, *P* precontrast phase, *V* venous phase. Normally distributed data (*k*-V, *k*-D) were analyzed by Student's *t* test, and were expressed as means ± standard deviations. Non-normally distributed data (NIC-A, NIC-V, NIC-D, Eff-Z, *k*-P, *k*-A) were analyzed by Mann-Whitney *U* test, and were expressed as medians and ranges (25th, 75th percentiles)

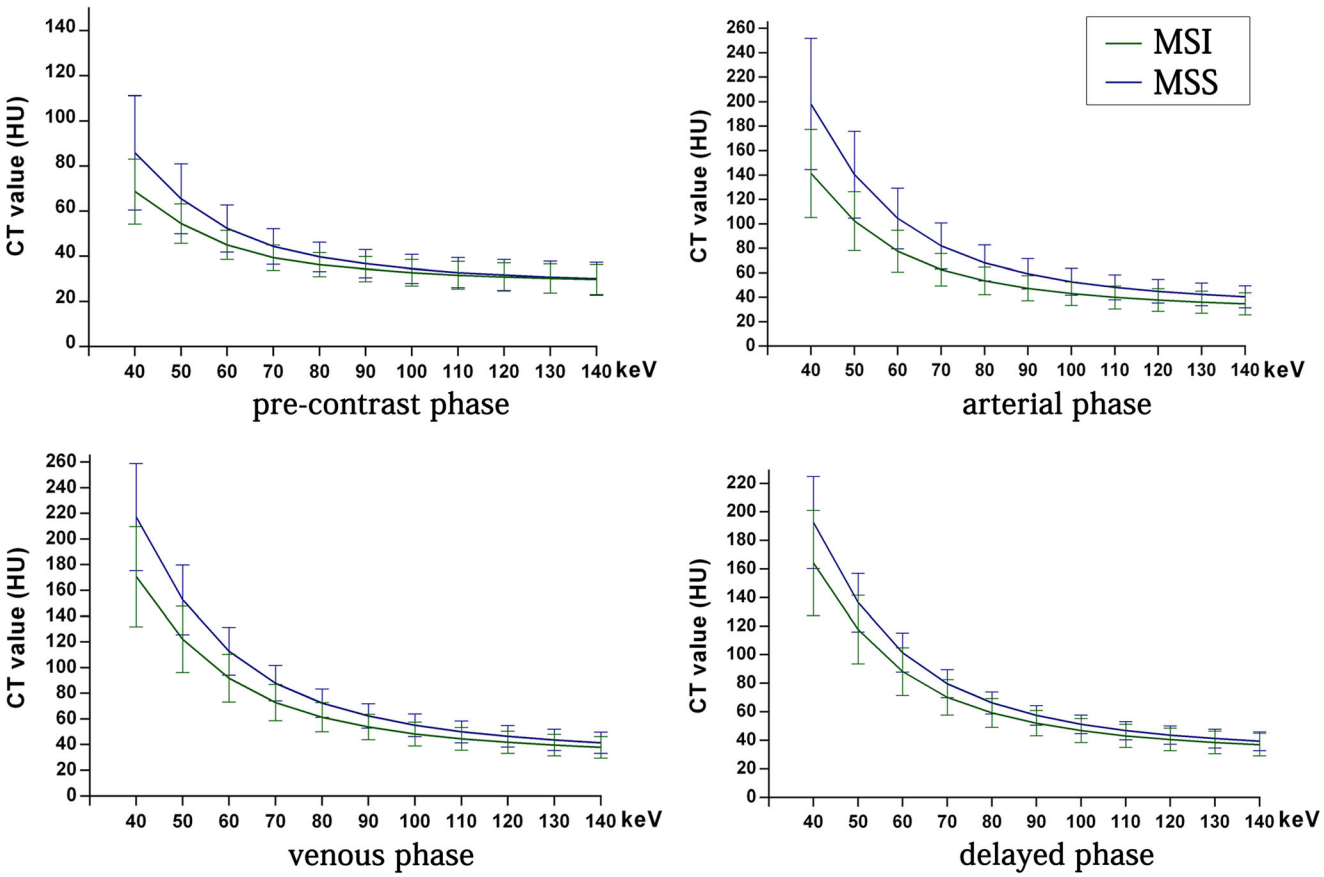

Fig. 4 The spectral Hounsfield unit curves between 40 and 140 keV. The slopes of curves in MSI CRC (green line) are significantly lower than those in MSS CRC (blue line) in the precontrast phase (0.557 vs 0.834, $p = 0.001$), arterial phase (1.513 vs 2.454, $p < 0.001$), venous phase (2.04 vs 2.70, $p < 0.001$), and delayed phase (1.96 vs 2.36, $p < 0.001$)

using NIC-A, NIC-V, NIC-D, and *k*-V (without statistical significance, $p = 0.165$, 0.456, 0.300, 0.617, respectively) (Table 3).

Combining statistically significant ssDECT parameters (NIC-A, NIC-V, NIC-D, Eff-Z, *k*-P, *k*-A, *k*-V, *k*-D) using multivariate logistic regression analysis (selection method, Enter) showed the optimal diagnostic capability for discriminating MSI from MSS CRC (AUC, 0.886; sensitivity, 81.6%; specificity, 81.6%). The AUC value, sensitivity, specificity, and 95% CI of combined parameters with different selection methods in multivariate logistic regression are shown in Supplementary Table 1.

The AUC of using combined parameters (obtained by multivariate logistic regression analysis; selection method, Enter) was significantly higher than using any other ssDECT parameter (NIC-A, $p = 0.003$; NIC-V, $p = 0.003$; NIC-D, $p = 0.001$; Eff-Z, $p < 0.001$; *k*-P, $p < 0.001$; *k*-A, $p = 0.009$; *k*-V, $p = 0.005$; *k*-D, $p < 0.001$). The ROC curves for discriminating MSI from MSS CRC are shown in Fig. 5.

Discussion

Our study revealed that the Eff-Z in the precontrast phase, the slopes of the spectral curves in precontrast phase, and all contrast-enhanced phases (*k*-C, A, V, D), and the NICs in all contrast-enhanced phases (NIC-A, V, D) derived from ssDECT imaging were all associated with MSI status in CRC patients. The combination of multiple parameters in ssDECT imaging provided relatively high diagnostic accuracy for discriminating MSI from MSS CRC.

The ssDECT imaging provides multiple parameters to be used as analytical tools and quantitative indicators [17, 18]. Eff-Z reflects the atomic number of the compound material; the denser the compound, the higher the effective atomic number [19]. In our study, we found that Eff-Z in the MSI CRC was statistically lower than that in MSS CRC ($p = 0.001$), and the changes of CT value as function energy in the precontrast phase (slope *k*-P) were also different between MSI and MSS CRC ($p = 0.001$). These differences may be explained by the various anatomic structures of MSI and MSS CRC, which are caused by the heterogeneous density of cellular components [14]. Previous studies have suggested that higher apoptosis/proliferation ratios, less actively proliferating tumor cells, more conspicuous infiltrating lymphocytes, and more morphological patterns (such as glandular, mucinous, and solid) were pathological characteristics of MSI tumors [15, 20–23]. However, the diagnostic value of Eff-Z was not very high: the AUC was only 0.69 with low sensitivity of 64.5%, and specificity of 64.8%. Similarly, the diagnostic value of the slope *k* of HU curve in the precontrast phase was quite low with AUC of 0.696. Hence, our results indicated that even though the anatomic structures of MSI and MSS tissues might be different, these differences had low separating power of MSI from MSS CRC, which may indicate that non-contrast CT alone are not sufficient clinically.

Iodine concentration can obviously reflect the vascularization in various tissues [24, 25]. Previous studies have shown that CRCs with different MSI status are associated with different degrees of vascularization. The lower microvessel density of the tumor and lower vascular endothelial growth factor expression have been suggested as phenotypic features of MSI tumors [13, 26, 27]. In our study, we found that the MSI CRC had significantly lower NIC values, suggesting less blood supply

Table 3 AUC value, sensitivity, specificity, cutoff value, and 95% CI in each parameter for differentiating MSI from MSS CRC

Parameters	AUC	Sensitivity	Specificity	Cutoff value	95% CI	*p* value
NIC-A	0.761	75%	71.1%	0.12	0.671–0.852	< 0.001
NIC-V	0.771	56.6%	86.8%	0.50	0.684–0.857	< 0.001
NIC-D	0.752	50%	89.5%	0.70	0.661–0.842	< 0.001
Eff-Z	0.690	64.5%	64.8%	7.98	0.594–0.787	0.001
k-P	0.696	40.8%	97.4%	0.96	0.600–0.792	0.001
k-A	0.803	72.4%	76.3%	2.00	0.724–0.882	< 0.001
k-V	0.784	82.9%	63.2%	2.13	0.694–0.874	< 0.001
k-D	0.703	71.1%	63.2%	2.08	0.602–0.803	< 0.001
Combined (CT)	0.886*	81.6%	81.6%	0.63#	0.823–0.949	< 0.001

A arterial phase, *AUC* area under the curve, *CI* confidence interval, *D* delayed phase, *Eff-Z* effective atomic numbers, *k* slope, *MSI* microsatellite instability, *MSS* microsatellite stability, *NIC* normalized iodine concentration, *P* precontrast phase, *V* venous phase

Combined (CT): all statistically significant ssDECT parameters (NIC-A, NIC-V, NIC-D, Eff-Z, *k*-P, *k*-A, *k*-V, *k*-D) were combined with multivariate logistic regression (selection method, Enter)

*The AUC when using combined ssDECT parameters was significantly higher than using any other ssDECT parameter (all $p < 0.05$)

#Probability value comes from multivariate logistic regression

for MSI tumors than for MSS tumors. Since the iodine-based material decomposition images reflect the uptake and clearance of iodine over time in arterial, venous, and delayed phase, we analyzed the three enhanced phases in our study. We found the diagnostic performance of NIC value in the arterial phase was relatively high: the AUC was 0.761 with sensitivity of 75%, and specificity of 71.1%. Conversely, the NIC in venous and delayed phase had no value to separate MSI from MSS CRC (with sensitivity of 56.6% and 50%).

While IC is static and reflects the amount of iodine in the tumors, the spectral curve indicates the attenuation changes of the tumor when being enhanced by contrast. The faster the spectral curve changes, the higher percentage of contrast medium (iodine) in the tumors. Previous studies have shown that lower angiogenesis has been observed in MSI tumors, and it may explain the differences and diagnostic accuracy of HU curve slope between the two types of tumors in enhanced phases. The spectral CT curve also has the flexibility to allow the selection of different segments of the curve for improving the sensitivity for measuring attenuation changes as photon energy [28]. In our study, we selected the energy range of 40–100 keV to measure the attenuation change (slope *k*) and found that this value had the highest discriminating power for differentiation between MSI and MSS tumors. From our results, we found that the slope *k* of the arterial phase had a higher diagnostic value (AUC 0.803; sensitivity, 72.4%; specificity, 76.3%; cutoff value, 2.00) than that of the venous and delayed.

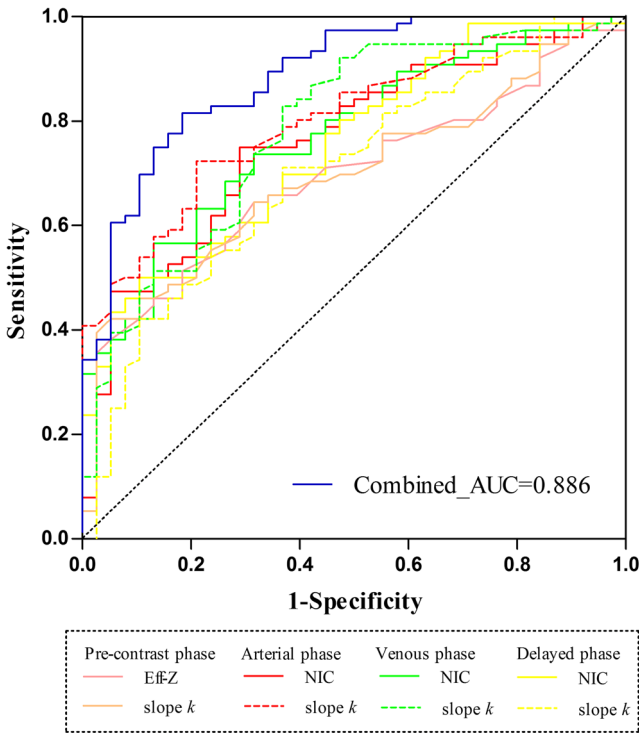

Fig. 5 ROC curves for discriminating MSI from MSS CRC by using effective atomic number (Eff-Z) in precontrast phase, slope *k* of the spectral curve in precontrast phase and all contrast-enhanced phases, and normalized iodine concentration (NIC) in all contrast-enhanced phases. The multivariate logistic regression (selection method, Enter) with combined ssDECT parameters improved diagnostic capability with AUC of 0.886 (sensitivity, 81.6%; specificity, 81.6%)

Previous studies tried to find imaging biomarkers to preoperatively evaluate MSI status, based on magnetic resonance imaging (MRI) and positron emission tomography/computed tomography (PET-CT) [29–31]. Bhosale et al analyzed the reduced field-of-view diffusion intra-voxel incoherent motion imaging on 12 stage I endometrial cancer patients, and the results showed that MSS tumors had a significantly higher apparent diffusion coefficient and true diffusion coefficient than MSI tumors. The difference may be caused by various densities of tumor cells [29]. Hong et al investigated the value of dynamic contrast-enhanced magnetic resonance imaging (DCE-MRI) to identify MSI status in rectal cancer; however, there were no significant correlations between MSI status and semiquantitative parameters of DCE-MRI, including steepest slope, time to peak, relative enhancement during a rapid rise, and maximal enhancement [30]. For gastric cancer, the correlations between MSI status and degrees of 18F-fluorodeoxyglucose uptakes were analyzed on PET-CT. Higher 18F-fluorodeoxyglucose uptake was observed in MSI gastric tumors and it was explained by more mucosal inflammation than in MSS tumors [31].

Our study has several limitations. First, the MSI status was tested via IHC staining in our study. Although it has been reported that IHC is a reliable method to assess MSI status, there is no denying that PCR is still the gold standard and should be recommended. Second, we could not make a complete match between the ROIs and the pathological specimen, although we had made efforts to minimize the bias by using two radiologists. Third, the number of patients in this study was limited, and further validation is required by using a larger sample. Fourth, although the parameter of ssDECT imaging may serve as imaging marker for discriminating MSI from MSS CRC, it is not ready to replace the pathological analysis.

In conclusion, our study suggested that the multiple parameters in ssDECT imaging may serve as imaging markers, and their combination by multivariate logistic regression may provide relatively high diagnostic accuracy for discriminating MSI from MSS CRC.

Funding This work was supported by the Program for Training Capital Science and Technology Leading Talents (No. Z181100006318003).

Compliance with ethical standards

Guarantor The scientific guarantor of this publication is Ailian Liu.

Conflict of interest The authors of this manuscript declare no relationships with any companies whose products or services may be related to the subject matter of the article.

Statistics and biometry No complex statistical methods were necessary for this paper.

Informed consent The informed consent was waived by the Institutional Review Board due to its retrospective design.

Ethical approval This retrospective study was approved by the Institutional Ethics Committee of the First Affiliated Hospital of Dalian Medical University (Dalian, China) and was performed in accordance with the ethical guidelines of the Declaration of Helsinki.

Methodology
- Retrospective
- Observational
- Performed at one institution

References

1. Siegel RL, Miller KD, Fedewa SA et al (2017) Colorectal cancer statistics, 2017. CA Cancer J Clin 67:104–117
2. Sinicrope FA (2018) Evaluation of the combined variable of MSI and BRAF with prognosis in colorectal cancer. Clin Gastroenterol Hepatol. https://doi.org/10.1016/j.cgh.2018.06.038
3. Gelsomino F, Barbolini M, Spallanzani A, Pugliese G, Cascinu S (2016) The evolving role of microsatellite instability in colorectal cancer: a review. Cancer Treat Rev 51:19–26
4. Benson AB 3rd, Venook AP, Cederquist L et al (2017) Colon cancer, version 1.2017, NCCN clinical practice guidelines in oncology. J Natl Compr Canc Netw 15:370–398
5. Passardi A, Canale M, Valgiusti M, Ulivi P (2017) Immune checkpoints as a target for colorectal cancer treatment. Int J Mol Sci 18(6):1324
6. Ryan E, Sheahan K, Creavin B, Mohan HM, Winter DC (2017) The current value of determining the mismatch repair status of colorectal cancer: a rationale for routine testing. Crit Rev Oncol Hematol 116:38–57
7. Árnadóttir S, Jeppesen M, Lamy P et al (2018) Characterization of genetic intratumor heterogeneity in colorectal cancer and matching patient-derived spheroid cultures. Mol Oncol 12:132–147
8. Marin D, Boll D, Mileto A, Nelson R (2014) State of the art: dual-energy CT of the abdomen. Radiology 271:327–342
9. Alnajami I, Drue HC, Steele R, Baatrup G (2017) Dual energy CT - a possible new method to assess regression of rectal cancers after neoadjuvant treatment. J Surg Oncol 116(8):984–988
10. Gong H, Zhang K, Wu L et al (2016) Dual energy spectral CT imaging for colorectal cancer grading: a preliminary study. PLoS One 11:e0147756
11. Fan S, Li X, Zheng L, Hu D, Ren X, Ye Z (2017) Correlations between the iodine concentrations from dual energy computed tomography and molecular markers Ki-67 and HIF-1α in rectal cancer: a preliminary study. Eur J Radiol 96:109
12. Kang HJ, Kim SH, Bae JS, Sun KJ, Han JK (2018) Can quantitative iodine parameters on DECT replace perfusion CT parameters in colorectal cancers? Eur Radiol 28(11):4775–4782
13. Hollingsworth SJ, Drye ER, Tou SI, Boulos PB (2005) Expression of angiogenic VEGF-A (soluble isoforms 121, 165) and lymphangiogenic VEGF-C in colorectal cancers with microsatellite instability. J Surg Oncol 92(4):317–325
14. De Smedt L, Lemahieu J, Palmans S et al (2015) Microsatellite instable vs stable colon carcinomas: analysis of tumour heterogeneity, inflammation and angiogenesis. Br J Cancer 113(3):500–509
15. Toh J, Chapuis P, Bokey L, Chan C, Spring K, Dent OF (2017) Competing risks analysis of microsatellite instability as a prognostic factor in colorectal cancer. Br J Surg 104:1250–1259
16. Rigau V, Sebbagh N, Olschwang S et al (2003) Microsatellite instability in colorectal carcinoma. The comparison of immunohistochemistry and molecular biology suggests a role for hMSH6 [correction of hMLH6] immunostaining. Arch Pathol Lab Med 127:694–700
17. Cui Y, Gao S, Wang Z et al (2012) Which should be the routine cross-sectional reconstruction mode in spectral CT imaging: monochromatic or polychromatic? Br J Radiol 85:e887–e890
18. Li M, Zhang L, Tang W, Jin YJ, Qi LL, Wu N (2018) Identification of epidermal growth factor receptor mutations in pulmonary adenocarcinoma using dual-energy spectral computed tomography. Eur Radiol 2018:1–9
19. Mileto A, Allen BC, Pietryga JA et al (2017) Characterization of incidental renal mass with dual-energy CT: diagnostic accuracy of effective atomic number maps for discriminating nonenhancing cysts from enhancing masses. AJR Am J Roentgenol 209(4):W221–W230
20. Sinicrope FA, Rego RL, Garrity-Park MM et al (2007) Alterations in cell proliferation and apoptosis in colon cancers with microsatellite instability. Int J Cancer 2007:1232–1238
21. Bernal M, Concha A, Sáenz-López P et al (2011) Leukocyte infiltrate in gastrointestinal adenocarcinomas is strongly associated with tumor microsatellite instability but not with tumor immunogenicity. Cancer Immunol Immunother 60(6):869–882
22. Lee SY, Miyai K, Han HS et al (2012) Microsatellite instability, EMAST, and morphology associations with T cell infiltration in colorectal neoplasia. Dig Dis Sci 57(1):72–78
23. Maby P, Tougeron D, Hamieh M et al (2015) Correlation between density of CD8+ T-cell infiltrate in microsatellite unstable colorectal cancers and frameshift mutations: a rationale for personalized immunotherapy. Cancer Res 75(17):3446–3455
24. Apfaltrer P, Meyer M, Meier C et al (2012) Contrast-enhanced dual-energy CT of gastrointestinal stromal tumors: is iodine-related attenuation a potential indicator of tumor response? Invest Radiol 47:65–70
25. Mirus M, Tokalov SV, Wolf G, Heinold J, Prochnow V, Abolmaali N (2017) Noninvasive assessment and quantification of tumour vascularisation using MRI and CT in a tumour model with modifiable angiogenesis - an animal experimental prospective cohort study. Eur Radiol Exp 1:15
26. Wynter CV, Simms LA, Buttenshaw RL et al (2015) Angiogenic factor VEGF is decreased in human colorectal neoplasms showing DNA microsatellite instability. J Pathol 189(3):319–325
27. Miyamoto N, Yamamoto H, Taniguchi H et al (2007) Differential expression of angiogenesis-related genes in human gastric cancers with and those without high-frequency microsatellite instability. Cancer Lett 254(1):42–53
28. Ajmi EA, Forghani B, Reinhold C, Bayat M, Forghani R (2018) Spectral multi-energy CT texture analysis with machine learning for tissue classification: an investigation using classification of benign parotid tumours as a testing paradigm. Eur Radiol 28(6):2604–2611
29. Bhosale P, Ramalingam P, Ma J et al (2017) Can reduced field-of-view diffusion sequence help assess microsatellite instability in FIGO stage 1 endometrial cancer? J Magn Reson Imaging 45:1216–1224
30. Hong H, Kim S, Park H et al (2013) Correlations of dynamic contrast-enhanced magnetic resonance imaging with morphologic, angiogenic, and molecular prognostic factors in rectal cancer. Yonsei Med J 54:123–130
31. Chung H, Lee S, Han H et al (2013) Gastric cancers with microsatellite instability exhibit high fluorodeoxyglucose uptake on positron emission tomography. Gastric Cancer 16:185–192